Nanoscale Advances

ROYAL SOCIETY OF CHEMISTRY

PAPER

View Article Online
View Journal | View Issue

Cite this: *Nanoscale Adv.*, 2021, **3**, 4851

One-pot construction of robust BiOCl/ZnO p–n heterojunctions with semi-coherent interfaces toward improving charge separation for photodegradation enhancement†

Xiaoli Yang, Shaodong Sun, * Jie Cui, Man Yang,* Qing Yang, Peng Xiao and Shuhua Liang*

Heterojunction engineering is an effective strategy to enhance the photodegradation activity *via* improving the spatial charge separation. However, the poor interface interactions and stability limit the photocatalytic activity and stability of traditional heterojunctions. Herein, robust BiOCl/ZnO p–n heterojunctions with semi-coherent interfaces were prepared by a one-pot hydrothermal method to improve the activity and stability toward photocatalytic degradation than that of the counterpart, in which the semi-coherent interfaces exhibited lower phase boundary energy, resulting in highly-stable interfaces between BiOCl and ZnO as well as the formation of the built-in electric field in this robust p–n heterojunction for enhanced charge separation. The cycle test results verified that the BiOCl/ZnO heterojunctions with semi-coherent interfaces can maintain the photocatalytic degradation activity at the initial level even after 10 cycles, while deactivation of the sample without semi-coherent interfaces occurred after 3 cycles only. Optical and electrical properties revealed that BiOCl/ZnO heterojunctions with semi-coherent interfaces possessed the highest electron migration and charge separation efficiency, resulting in the highest photodegradation activity. Density functional theory (DFT) calculations and electron spin-resonance (ESR) results verified that the enhanced charge separation was assigned to the type-II photocatalytic mechanism, leading to the enhancement of $^{\bullet}OH$ and $^{\bullet}O_2^-$ reactive oxygen species. This work would provoke the development of one-step construction of new highly active BiOX (X = Cl, Br, and I)-based heterogeneous photocatalysts with stable semi-coherent interfaces.

Received 28th May 2021
Accepted 6th July 2021

DOI: 10.1039/d1na00396h

rsc.li/nanoscale-advances

1. Introduction

Photocatalysis has been regarded as a green technology that converts solar energy to chemical energy, which is widely employed in organic pollutant degradation,[1–3] water splitting,[4,5] carbon dioxide reduction,[5–8] and ammonia synthesis.[9,10] Charge separation in a semiconductor is one of the crucial factors affecting energy conversion efficiency. However, the photo-generated electrons (e^-) and holes (h^+) recombine easily and cannot efficiently transfer to the surface reactive sites for redox reaction in general. In the past few years, many approaches have been made to improve the surface charge separation, such as noble metal deposition,[11,12] heterojunction[13–15] and defect engineering.[16–18] In particular, the construction of a heterojunction is effective to limit the recombination of photogenerated e^- and h^+ and thereby enhance the photocatalytic activity. Heterojunction integration of p-type and n-type semiconductors with suitable band edge positions has been confirmed to be positive for spatial charge separation.[19,20] For example, Hou and co-workers have reported $Bi_4Ti_3O_{12}$/BiOI p–n junctions, which exhibited a superior photodegradation activity for rhodamine B (RhB) and phenol to pure $Bi_4Ti_3O_{12}$ and BiOI, respectively.[21] Similarly, other types of bismuth oxyhalide (BiOX, X = Cl, Br and I) p–n heterojunction photocatalysts have also been constructed, such as BiOBr/$La_2Ti_2O_7$,[22] BiOI/g-C_3N_4,[23] and BiOI/$KTaO_3$.[24] As a result, integrating p-type BiOX and n-type semiconductor into a heterojunction is a valid way to increase the migration of photogenerated e^- and h^+ to the opposite semiconductors with a low conductive band (CB) and high valence band (VB), respectively, finally resulting in the improvement of charge separation.

Because the redox potentials play an important role in spatial charge separation for a heterojunction,[25,26] the

Engineering Research Center of Conducting Materials and Composite Technology, Ministry of Education, Shaanxi Engineering Research Centers of Metal-Based Heterogeneous Materials and Advanced Manufacturing Technology, Shaanxi Province Key Laboratory for Electrical Materials and Infiltration Technology, School of Materials Science and Engineering, Xi'an University of Technology, Xi'an 710048, Shaanxi, People's Republic of China. E-mail: sdsun@xaut.edu.cn; myang@xaut.edu.cn; liangsh@xaut.edu.cn

† Electronic supplementary information (ESI) available: Additional XRD, SEM, DRS and photocatalytic degradation curves of RhB solution. See DOI: 10.1039/d1na00396h

composition of the n-type semiconductor building block in a BiOX-based p–n heterojunction is crucial to achieving the high photocatalytic performance. If an n-type ZnO semiconductor with high oxidation potential[27–29] is incorporated into the as-mentioned BiOCl with high oxidation potential, the separation efficiency of photogenerated e^- and h^+ would be highly improved due to the formation of a p–n heterojunction. For instance, Vaizoğullar *et al.* have fabricated BiOCl/ZnO/Bent materials with an effective degradation of 3-chlorophenol (3-CP) by a successive synthesis method.[30] Similarly, Zhang *et al.* have demonstrated that BiOCl/ZnO/C_3N_4 photocatalyst exhibited superior photodegradation performance for RhB and methyl orange (MO) to BiOCl/ZnO, BiOCl and C_3N_4.[31] Additionally, Liu *et al.* have prepared BiOCl/ZnO heterostructures with oxygen-rich vacancies using a one-step microwave technique, which can effectively enhance photocatalytic performance for the degradation of tetracycline hydrochloride (TC-HCl) than those of pure BiOCl and ZnO. This study showed that oxygen vacancy and interfacial electric field derived from heterostructures were responsible for the improvement of light harvesting and the separation efficiency of photogenerated charge carriers.[32] However, there are still some drawbacks, such as the poor-matched interface and poor stability as well as complex fabrication strategy in the current BiOCl/ZnO-based heterojunctions. Therefore, it is meaningful to explore a new method for promoting the interface interaction and stability in a BiOCl/ZnO heterojunction.

Herein, we present a novel one-pot hydrothermal strategy for the synthesis of robust BiOCl/ZnO heterojunctions with semi-coherent interfaces and compare the stability of catalysts fabricated by the above strategy with the successive process method. As expected, the well-matched BiOCl/ZnO heterojunctions exhibit significantly higher photocatalytic activities toward the degradation of RhB and tetracycline (TC) as well as ciprofloxacin (CIP) solution than the sample prepared by the successive synthesis method, which can be attributed to the formation of the built-in electric field in the robust p–n heterojunction for improved charge separation. Significantly, the cycle test results confirm that the BiOCl/ZnO heterojunctions with semi-coherent interfaces synthesized by the one-step hydrothermal method maintain the photocatalytic degradation activity at the initial level even after the 10^{th} cycle, while deactivation of the sample without semi-coherent interfaces prepared by a successive process occurred after the 3^{rd} cycle only. The enhanced photocatalytic mechanism was proposed in detail based on the systematic characterizations and density functional theory (DFT) calculations, which belonged to the type-II pathway. This work might provide a theoretical reference for the one-pot construction of new heterogeneous photocatalysts with well-matched interfaces.

2. Experimental

2.1. Sample preparation

BiOCl/ZnO heterojunctions were produced by a one-pot hydrothermal method. Typically, 1 mmol $ZnCl_2$ (Sinopharm Chemical Reagent Co, Ltd, China), 0.6 mmol $Na_2SnO_3 \cdot 3H_2O$ (Aldrich Chemistry Technology Co, Ltd, Germany), and different amounts (1 mmol, 2 mmol, 4 mmol) $Bi(NO_3)_3 \cdot 5H_2O$ (Shanghai Aladdin Bio-Chem Technology Co, Ltd, China) were dissolved in deionized water, respectively. Subsequently, the above solutions were put in a 100 mL Teflon-lined stainless-steel autoclave under constant stirring at room temperature. After stirring for 30 min, the autoclave was treated at 200 °C for 12 h in an oven and then cooled down to ambient temperature. The products were obtained by centrifugation and washed with water and absolute ethanol three times and once, followed by drying at 60 °C for 12 h in an oven. The resultant catalysts were denoted as ZTO, BZ-0.5, BZ-0.67, BZ-0.8, and BiOCl, according to the mole ratios of the added Bi/(Bi + Zn), 0, 0.5, 0.67, 0.8 and 1, respectively.

2.2. Characterizations

The powder X-ray diffraction (XRD) patterns were acquired on the Bruker-AXS D8 ADVANCE X-ray diffractometer equipped with Cu Kα radiation source (λ = 1.54 Å). Scanning electron microscope (SEM) images were observed on the JEOL (JSM-7000F) instrument operated at 15 kV and equipped with an energy dispersive spectrometer (EDS) microanalysis system. Transmission electron microscopy (TEM) images were investigated using the JEOL (JEM-2100) instrument operated at 200 kV. Electron spin-resonance (ESR) experiments were conducted on a Bruker-EMX nano with 5,5-dimethyl-1-pyrroline-*N*-oxide (DMPO). UV-vis diffuse reflectance spectra (DRS) were acquired on a Hitachi U-4100 apparatus furnished with an integrated sphere attachment with $BaSO_4$ as the reference. Room temperature fluorescence emission spectra (PL) were obtained on FluoroLog-3, HORIBA, Jobin Yvon fluorescence spectrophotometer. The photocurrent was obtained on Shanghai Chenhua electrochemical system (CHI660E). The Xe lamp (300 W) was used to provide full spectrum irradiation. The reference electrode and the counter electrode were saturated calomel electrode and Pt wire, respectively. The working electrode was prepared as follows: initially, 0.01 g catalyst and 1 mL ultrapure water were mixed. Then, 20 μL Nafion was added into the above mixture and ultrasound dissolved for 15 min. Finally, the mixture was dropped on a 10 mm × 20 mm indium tin oxide (ITO) glass, which was sealed with scotch tape, dried at 60 °C for 12 h, and calcined at 100 °C for 1 h. The electrolyte solution was 150 mL 0.2 M Na_2SO_4 aqueous solution.

2.3. Photocatalytic performance

The detailed process of the photocatalytic degradation of RhB, TC, and CIP solution is shown below. For degradation of the RhB solution, 10 mg photocatalyst was put into RhB aqueous solution (5 mg L^{-1}, 50 mL) and stirred under 600 rpm for 1 h in darkness. Then, the mixture was continuously stirred in the full spectrum from a 300 W Xe lamp at room temperature. The RhB solution was centrifugated every 4 min and analyzed by UV-vis spectra. For the degradation of TC or CIP solution, 10 mg BiOCl/ZnO photocatalyst was put into TC or CIP aqueous solution (20 mg L^{-1}, 50 mL), and the subsequent procedures

were similar to the above process. The degradation efficiency was obtained using the following equations:

$$\text{Degradation efficiency} = \frac{C_0 - C}{C_0} \times 100\%$$

C_0: the initial absorbance, C: the absorbance at a specific time.

3. Results and discussion

The BiOCl/ZnO heterojunctions were prepared by mixing $ZnCl_2$, Na_2SnO_3, and $Bi(NO_3)_3$ aqueous solution followed by hydrothermal treatment (Fig. 1). In an aqueous environment, $ZnCl_2$ existed in the form of zinc and chloride ions. The zinc ions can react with the hydroxyl ions originating from the hydrolysis of Na_2SnO_3, leading to the formation of $Zn(OH)_2$, which can be decomposed into ZnO species under hydrothermal conditions. Meanwhile, the chloride ions would react with BiO^+ ions generated from the hydrolysis of $Bi(NO_3)_3$, resulting in the formation of BiOCl. The detailed reaction equations are given in the inset of Fig. 1. Thus the one-pot construction of robust BiOCl/ZnO p–n heterojunctions was achieved under hydrothermal conditions. The interfaces between BiOCl and ZnO might be well-matched because of the simultaneous coprecipitation and ripening. In this work, the resultant catalysts had a Bi/(Bi + Zn) mole ratio of 0, 0.5, 0.67, 0.8, and 1, and they were denoted ZTO, BZ-0.5, BZ-0.67, BZ-0.8, and BiOCl, respectively.

In order to confirm the crystal phases of these photocatalysts, XRD was performed. As shown in Fig. 2, the XRD spectrum of the BZ-0.67 sample displayed the diffraction peaks located at (002), (101), (102), (112), (200), (113), (211), (104), (212), (114), and (214) crystal planes, respectively, corresponding to the tetragonal BiOCl crystal phase (JCPDS No. 06-0249). The diffraction peaks of the ZnO crystal (JCPDS No. 75-1526) were also detected, which were indexed to (100), (002), (101), (102), (103), (112), (201), and (202) crystal planes. The results demonstrated that BiOCl and ZnO were synthesized successfully by this one-pot hydrothermal method. Moreover, when the Bi/(Bi + Zn) mole ratio is 1, the XRD pattern was in good accordance with BiOCl (JCPDS No. 06-0249) (Fig. S1(a)†). When the Bi/(Bi + Zn) mole ratio is 0, the XRD pattern could be indexed to the composite phase of Zn_2SnO_4 (JCPDS No. 24-1470) and $ZnSn(OH)_6$ (JCPDS No. 73-2384) (Fig. S1(b)†).

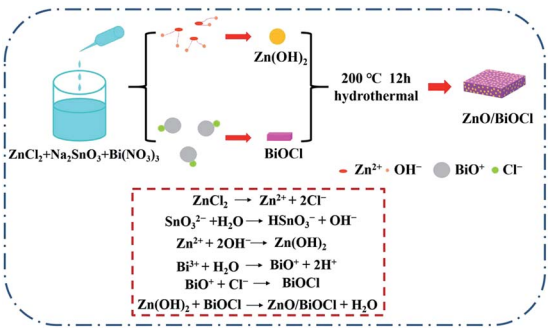

Fig. 1 Schematic illustration of the preparation pathway of BiOCl/ZnO heterojunctions.

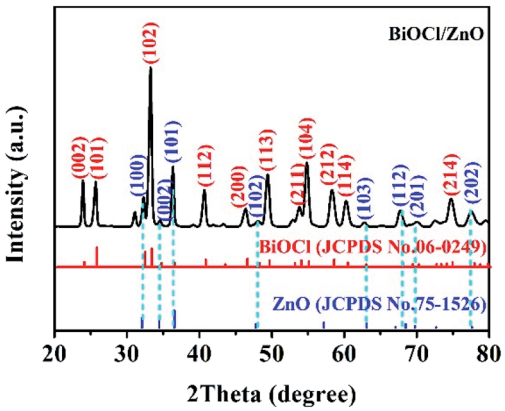

Fig. 2 XRD pattern of the as-prepared BZ-0.67 sample.

Scanning electron microscopy (SEM) and transmission electron microscopy (TEM) were employed to characterize the morphology and microstructure of BZ-0.67. As shown in the SEM images in Fig. 3, the BiOCl was composed of square-shaped nanosheets, while the abundant ZnO was well-dispersed on the surface of BiOCl as uniform nanoparticles. The results suggested the formation of BiOCl/ZnO heterojunctions. Notably, the pure BiOCl consisted of nanosheets, and the ZTO consisted of nanocubes, as given in Fig. S2.† The TEM of the top view (Fig. 4(a) and (b)) and the side view (Fig. 4(d)) images of BZ-0.67 further confirmed the ZnO nanoparticles were attached on the surface of the BiOCl nanosheet, indicating the BiOCl/ZnO heterojunction was constructed successfully, which was in good agreement with their SEM images. The selected area electron diffraction (SEAD) pattern displayed periodic diffraction spots with identified crystal planes of (200), (110), and $(1\bar{1}0)$ of tetragonal BiOCl as well as diffraction rings with crystal planes of (002) and (110) of hexagonal ZnO (Fig. 4(c)), indicating the formation of single-crystalline BiOCl and poly-crystalline ZnO, respectively. The results were in good agreement with the XRD pattern. High-resolution TEM (HRTEM) was also conducted to further clearly investigate the microstructure between BiOCl and ZnO interface of BZ-0.67. Fig. 4(e) showed the lattice fringe with spacings of 0.19 nm and 0.26 nm, corresponding to the (200) and (002) facets of BiOCl and ZnO, respectively. Particularly, the corresponding Inverse Fast Fourier Transform (IFFT) image exhibited a profound interfacial connection between BiOCl and ZnO in BZ-0.67 (Fig. 4(f)). The intimate interfacial connection between

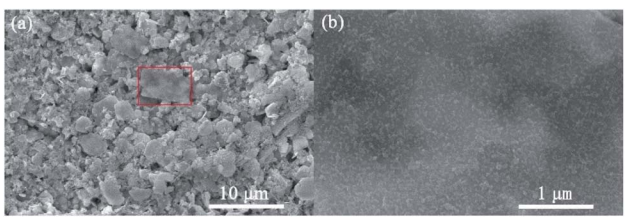

Fig. 3 (a) Low-magnification SEM image of BZ-0.67, (b) high-magnification of the rectangular section (red color) as shown in (a).

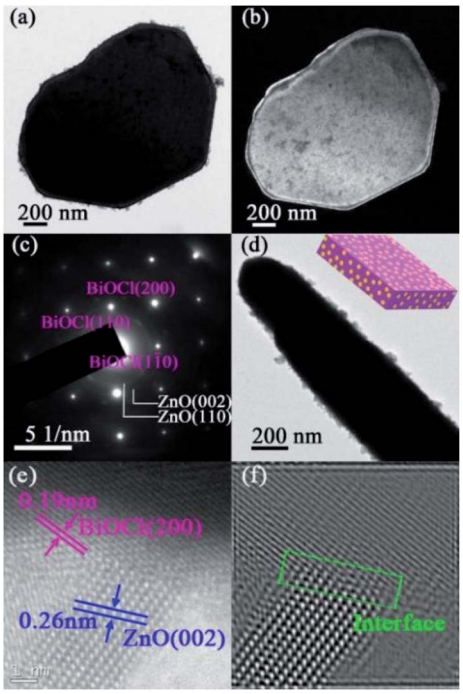

Fig. 4 (a and b) Bright-field and dark-field TEM images of the top views of BZ-0.67, respectively; (c) SAED pattern, (d) TEM image of a side view, (e) HRTEM image and (f) IFFT image. The inset of (d) is the corresponding schematic diagram.

BiOCl and ZnO leads to the establishment of the heterojunction. The HRTEM result clearly demonstrated an obvious semi-coherent interface between the BiOCl and ZnO heterojunction, rather than the simple physical mixture, which further confirmed the formation of the well-matched BiOCl/ZnO heterojunction.

To investigate the special photocatalytic activity and stability of BiOCl/ZnO heterojunctions with semi-coherent interfaces obtained from the one-pot preparation method, the BZ-0.67, BZ-0.67-S, ZTO, and BiOCl were selected to evaluate the photocatalytic degradation performance of RhB solution under a full spectrum illumination condition. Notably, the BZ-0.67-S was prepared by the successive synthesis method for comparison.[33] The XRD spectrum of BZ-0.67-S in Fig. S3† had similar characteristic peaks to the BZ-0.67, indicating that BiOCl and ZnO were constructed. SEM and TEM were employed to characterize the morphology and microstructure of BZ-0.67-S. The SEM images of BZ-0.67-S in Fig. S4† indicated the morphology of BiOCl was also the square-shaped nanosheets, and the ZnO nanoparticles were randomly dispersed on the surface of BiOCl nanosheets. However, the size of ZnO particles in BZ-0.67-S was larger than that in BZ-0.67, suggesting ZnO aggregates to larger particles by a successive synthesis process, which might decrease the active sites. From the TEM images of BZ-0.67-S in Fig. S5,† it can be seen that the interfaces between BiOCl and ZnO were physical contacts and incoherent, which indicated that an unmatchable BiOCl/ZnO heterojunction without semi-coherent interfaces was formed in BZ-0.67-S. The photocatalytic results are shown in Fig. 5(a) and (b), respectively. It

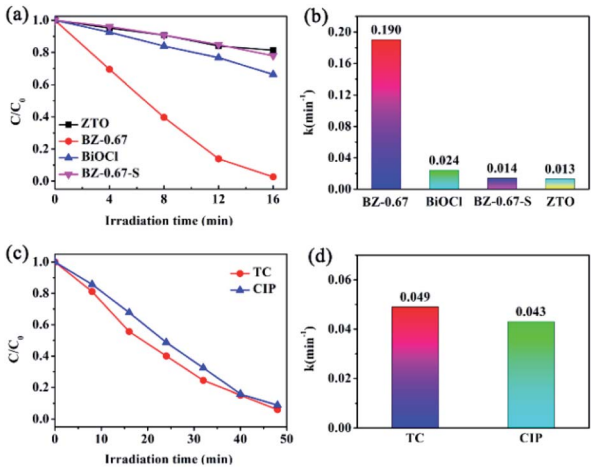

Fig. 5 (a and b) Photocatalytic degradation of RhB solution by BZ-0.67, BZ-0.67-S, ZTO, and BiOCl samples; (c and d) photocatalytic degradation of TC and CIP solution by BZ-0.67 sample.

was found that BZ-0.67 exhibited a much higher photocatalytic activity than those of the BZ-0.67-S, pure ZTO, and pure BiOCl. After 16 min, the RhB solution can be degraded to 99.7% of the initial concentration over BZ-0.67, while 22.1%, 18.6%, and 33.9% of the initial concentration over BZ-0.67-S, pure ZTO, and pure BiOCl, respectively. The apparent rate constants (k) of the photocatalytic reaction are 0.190, 0.014, 0.013, and 0.024 min^{-1} for BZ-0.67, BZ-0.67-S, pure ZTO, and pure BiOCl, respectively. The catalysts prepared by the one-pot hydrothermal method with various Bi/(Bi + Zn) mole ratios were also employed for the photocatalytic degradation of RhB. The results demonstrated that BZ-0.67 displayed superior photocatalytic activity in comparison to other samples (Fig. S6†). Besides, we have compared the photocatalytic performance of BZ-0.67 with other BiOCl/ZnO catalysts reported in the literatures (Table S1†). One can see that the BZ-0.67 in our work exhibits a relatively high activity among BiOCl/ZnO catalysts reported in the literature. Furthermore, to eliminate the sensitization effect of RhB on photocatalysis, photocatalytic degradation of TC and CIP were evaluated over BZ-0.67. It was found that BZ-0.67 possessed excellent photocatalytic degradation activities for both TC and CIP (Fig. 5(c) and (d)), suggesting it is photocatalysis rather than photosensitization for dye degradation over BZ-0.67. These results indicate that the construction of robust BiOCl/ZnO heterojunction can accelerate the charge separation and transfer than pure BiOCl and ZnO. Moreover, the preparation methods have an obvious influence on photocatalytic activity. The heterojunction prepared by the one-pot method (BZ-0.67) is much better matched and preferable to the charge separation and transfer than that prepared by the successive synthesis method (BZ-0.67-S).

In order to further investigate the photocatalytic stabilities of BZ-0.67 and BZ-0.67-S, cycle tests were performed. As shown in Fig. 6, the BZ-0.67 almost maintained its photocatalytic degradation activity of RhB at the initial level even after 10 cycles. In contrast, the BZ-0.67-S nearly lost two-thirds photocatalytic degradation activity of RhB at the initial level after 3 recycles.

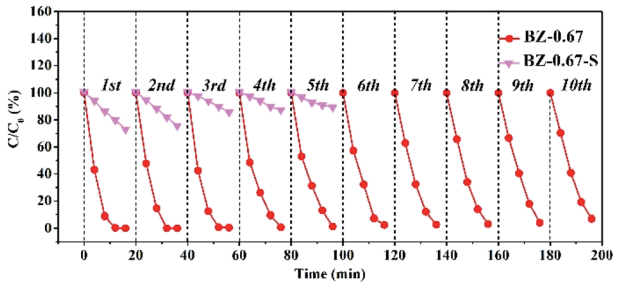

Fig. 6 The cycling degradation activity of BZ-0.67 and BZ-0.67-S.

Notably, a series of characterizations of BZ-0.67 after the recycling test was carried out. Both the SEM image and XRD pattern demonstrated that the structure of BZ-0.67 did not change before and after the recycling test (Fig. S7†). The ICP results of the solution after the cycle test in Table S2† demonstrated that no metal was leached after catalytic reaction, further demonstrating the stability of BZ-0.67. These results proved excellent photocatalytic stability of BZ-0.67 with the well-matched semicoherent interfaces between BiOCl and ZnO in heterojunction.

The optical and electrical properties were conducted to examine the separation of intrinsic photoinduced charge carriers in BiOCl/ZnO heterojunction. As displayed in Fig. 7(a), the BZ-0.67 presented a distinctly higher photocurrent density than BZ-0.67-S, pure ZTO, and pure BiOCl. The results indicated that the BZ-0.67 heterojunctions possessed the highest electron–hole separation efficiency, which was consistent with the trend of photocatalytic activities. In addition, the intrinsic band-edge PL was conducted to detect the recombination of photogenerated electrons and holes. The weakest photoluminescence (PL) quenching of BZ-0.67 suggested that it had the least photogenerated charge recombination among the as-prepared catalysts, which was also in accordance with the trend of photocatalytic activities (Fig. 7(b)). Based on the above results, the BZ-0.67 heterojunction has the highest electron migration and charge separation efficiency for enhanced photocatalytic activity.

To understand the photocatalytic mechanism of the excellent performance over the BZ-0.67 heterojunction, the photocatalytic degradation activities were evaluated with different sacrificial reagents including ethanol (EA), tertiary butyl alcohol (TBA), and ascorbic acid (AA) for capturing h^+, $^{\cdot}OH$, and $^{\cdot}O_2^-$, respectively, in order to determine the active species

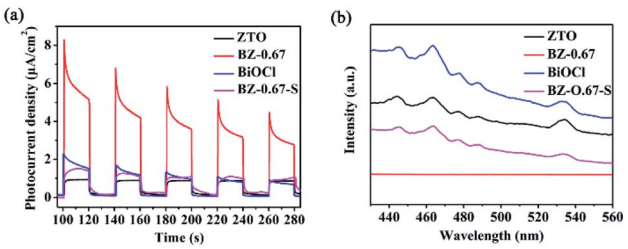

Fig. 7 (a) Photocurrent responses and (b) PL spectra of BZ-0.67, BZ-0.67-S, ZTO, and BiOCl samples.

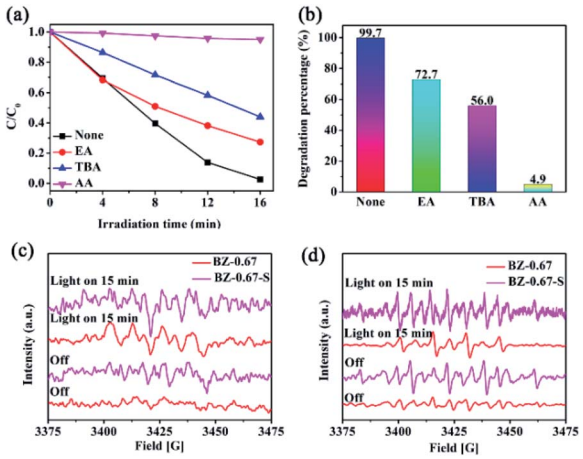

Fig. 8 (a and b) Inhibition effect of radical scavengers on RhB degradation in the BZ-0.67 sample; ESR spectra of $^{\cdot}O_2^-$ (c) and $^{\cdot}OH$ species (d) obtained from the BZ-0.67 and BZ-0.67-S in the presence of DMPO.

participating in the photodegradation reaction. As shown in Fig. 8(a) and (b), all three sacrificial agents have a certain inhibitory effect on the photocatalytic degradation activity of RhB in the BZ-0.67 catalyst system. However, in the presence of TBA and AA, the degradation activity decreased dramatically to 56.0% and 4.9% after 16 min, respectively. It proved that $^{\cdot}OH$ and $^{\cdot}O_2^-$ were generated and active for the degradation process. Besides, ESR measurement was conducted to confirm the existence of $^{\cdot}OH$ and $^{\cdot}O_2^-$. The 5,5-dimethyl-1-pyrroline (DMPO) was employed as the spin-trapping reagent for the capturing of $^{\cdot}OH$ and $^{\cdot}O_2^-$. As shown in Fig. 8(c) and (d), in the BZ-0.67 catalyst system, $^{\cdot}O_2^-$ signal and weak $^{\cdot}OH$ signal were detected, which proved that $^{\cdot}O_2^-$ was the main reactive oxygen species in BZ-0.67, and $^{\cdot}OH$ played the second important role in the degradation process. Obviously, it was found that both the $^{\cdot}O_2^-$ and $^{\cdot}OH$ signals were weaker in BZ-0.67-S than those of BZ-0.67, which meant that the BZ-0.67 heterojunction was beneficial to producing $^{\cdot}OH$ and $^{\cdot}O_2^-$ species than those in BZ-0.67-S.

DFT calculations were applied to further investigate the enhanced photocatalytic mechanism. The Fermi energy of BiOCl and ZnO were calculated as 5.30 eV and 4.68 eV, respectively (Fig. 9(a) and (b)). Besides, the CB potentials and the VB potentials of BiOCl and ZnO can be calculated by the following equations.[34]

$$E_{VB} = X - E^e + 0.5E_g$$

$$E_{CB} = E_{VB} - E_g$$

X represents the absolute electronegativity of the semiconductor (which is the geometric mean of the electronegativity of the constituent atoms), $X_{ZnO} = (X_{Zn} \times X_O)^{1/2} = 5.79$ eV, $X_{BiOCl} = (X_{Bi} \times X_O \times X_{Cl})^{1/3} = 6.65$ eV. E^e is on behalf of the energy of free electrons on the hydrogen scale around 4.5 eV. E_g value can be obtained from the UV-vis diffuse reflectance spectra (DRS) in Fig. S8.† Thus, the VB potentials of BiOCl and ZnO were calculated as 3.78 eV and 2.92 eV, and the CB potentials of

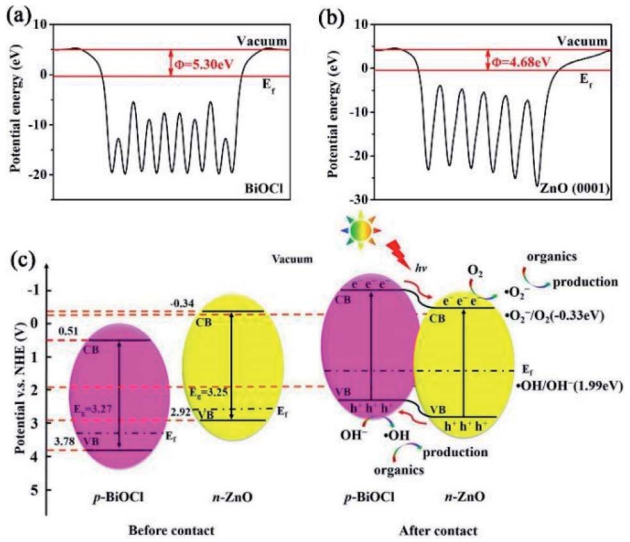

Fig. 9 The calculated Fermi energy of (a) BiOCl and (b) ZnO; (c) schematic diagram of the proposed mechanism for the photocatalytic degradation under light irradiation.

BiOCl and ZnO were calculated as 0.51 eV and −0.34 eV, respectively. Before contact, the Fermi energy level of p-type BiOCl and n-type ZnO are close to VB. After contact, the Fermi energy moved toward each other, and the transfer of electrons and holes would occur at the p–n heterojunction. Thus, a built-in electric field was formed, which could generate a strong driving force for facilitating electron transfer and separation. Therefore, when BiOCl and ZnO were in contact, a staggered band alignment (type II) structure was formed (Fig. 9(c)). Under light irradiation, the electrons in BiOCl migrated from VB to CB, and then transferred to the CB of ZnO because of the conduction band offset. Meanwhile, the holes on VB of ZnO were transferred to BiOCl and finally accumulated on the VB of BiOCl due to the valence band offset. Consequently, the internal electric field built in the p–n heterojunction of BiOCl/ZnO promoted the separation efficiency of photogenerated electrons–holes, leading to an extremely enhanced photocatalytic activity.

4. Conclusions

In summary, a robust BiOCl/ZnO p–n heterojunction with semi-coherent interfaces was prepared by a one-pot hydrothermal method, which exhibited remarkable catalytic performance and excellent stability toward the photodegradation of RhB, TC, and CIP than the sample prepared by the successive synthesis method. The distinct photoreactivity of BiOCl/ZnO was attributed to the built-in electric field in the p–n heterojunction for enhancing the separation of photogenerated electrons–holes, and the good photocatalytic stability was assigned to its lower phase boundary energy in a well-matched semi-coherent interface. This work demonstrates an effective strategy for resolving the drawbacks of poor interface interaction and stability in conventional heterojunctions, which would provoke the development of one-step construction of new highly active BiOX-based heterogeneous photocatalysts.

Conflicts of interest

The authors declare that there are no conflicts of interest.

Acknowledgements

This work was supported by the National Science Foundation of China (NSFC No. 51834009, 51801151 and U1866203), the Natural Science Foundation of Shaanxi Province (No. 2020JZ-47 and 2020JM-451), the Hundred Talent Program of Shaanxi Province, the Key Laboratory Project of Shaanxi Education Department (No. 18JS070, 18JK0560 and 17JS081), the Shaanxi Province Science Fund for Distinguished Young Scholars (2018JC-027), China Postdoctoral Science Foundation (Grant No. 2018M633643XB), the Key Research and Development Project of Shaanxi Province (No. 2017ZDXM-GY-033 and 2017ZDXM-GY-028), and the Key Laboratory Project of Science and Technology Agency (No. 13JS075).

Notes and references

1 S. D. Sun, J. Li, P. Song, J. Cui, Q. Yang, X. Zheng, Z. M. Yang and S. H. Liang, *Appl. Surf. Sci.*, 2020, **500**, 143985.
2 Y. Peng, Y. G. Mao and P. F. Kan, *CrystEngComm*, 2018, **20**, 7809–7817.
3 Y. Guo, Y. X. Dai, W. Zhao, H. Li, B. Xu and C. Sun, *Appl. Catal., B*, 2018, **237**, 273–287.
4 S. S. Yi, B. R. Wulan, J. M. Yan and Q. Jiang, *Adv. Funct. Mater.*, 2019, **29**, 1801902.
5 Z. L. Wang, J. J. Fan, B. Cheng, J. G. Yu and J. S. Xu, *Mater. Today Phys.*, 2020, **15**, 100279.
6 C. Chen, J. P. Jin, S. T. Chen, T. X. Wang, J. R. Xiao and T. Y. Peng, *Mater. Res. Bull.*, 2021, **137**, 111177.
7 M. L. Gu, Y. H. Li, M. Zhang, X. M. Zhang, Y. Shen, Y. Q. Liu and F. Dong, *Nano Energy*, 2021, **80**, 105415.
8 T. Butburee, Z. X. Sun, A. Centeno, F. Xie, Z. F. Zhao, D. X. Wu, P. Peerakiatkhajohn, S. Thaweesak, H. Q. Wang and L. Z. Wang, *Nano Energy*, 2019, **62**, 426–433.
9 D. N. Liu, J. H. Wang, S. Bian, Q. Liu, Y. H. Gao, X. Wang, K. Chu and X. F. Yu, *Adv. Funct. Mater.*, 2020, **30**, 2070156.
10 M. Liu, P. Wu, H. T. Li, Z. B. Chen, L. Z. Wang, X. Zeng, Y. X. Zhu, Y. J. Jiang, X. Z. Liao, S. Haynes, J. H. Ye, C. Stampfl and J. Huang, *Appl. Catal., B*, 2019, **259**, 118026.
11 J. J. Liu, Q. H. Yuan, H. T. Zhao and S. H. Zou, *Catal. Lett.*, 2018, **148**, 1093–1099.
12 L. L. Ling, Y. W. Feng, H. Li, Y. Chen, J. Y. Wen, J. Zhu and Z. F. Bian, *Appl. Surf. Sci.*, 2019, **483**, 772–778.
13 G. D. Fan, B. H. Du, J. J. Zhou, W. W. Yu, Z. Y. Chen and S. W. Yang, *Appl. Catal., B*, 2020, **265**, 118610.
14 S. J. Ye, M. Yan, X. F. Tan, J. Liang, G. M. Zeng, H. P. Wu, B. Song, C. Y. Zhou, Y. Yang and H. Wang, *Appl. Catal., B*, 2019, **250**, 78–88.

15 S. J. Ye, M. Cheng, G. M. Zeng, X. F. Tan, H. P. Wu, J. Liang, M. C. Shen, B. Song, J. Q. Liu, H. L. Yang and Y. F. Zhang, *Water Res.*, 2020, **179**, 115876.
16 J. Xiong, J. Di, J. Xia, W. Zhu and H. Li, *Adv. Funct. Mater.*, 2018, **28**, 1801983.
17 D. Zhang, G. Q. Tan, M. Wang, B. Lia, M. Y. Dang, H. J. Ren and A. Xia, *Appl. Surf. Sci.*, 2020, **526**, 146689.
18 W. D. Hou, J. Yang, H. M. Xu, D. Y. Li, Z. W. Zou and D. S. Xia, *CrystEngComm*, 2020, **22**, 3956–3964.
19 S. Bai, J. Jiang, Q. Zhang and Y. J. Xiong, *Chem. Soc. Rev.*, 2015, **44**, 2893–2939.
20 H. J. Lu, Q. Hao, T. Chen, L. H. Zhang, D. M. Chen, C. Ma, W. Q. Yao and Y. F. Zhu, *Appl. Catal., B*, 2018, **237**, 59–67.
21 D. F. Hou, X. L. Hu, P. Hu, W. Zhang, M. F. Zhang and Y. H. Huang, *Nanoscale*, 2013, **5**, 9764–9772.
22 Y. H. Ao, K. D. Wang, P. F. Wang, C. Wang and J. Hou, *Appl. Catal., B*, 2016, **194**, 157–168.
23 N. Tian, H. W. Huang, S. B. Wang, T. R. Zhang, X. Du and Y. H. Zhang, *Appl. Catal., B*, 2020, **267**, 118697.
24 X. X. Lu, Q. Li, S. H. Liu, R. Luo, H. Li, M. Zhang, C. P. Cui, G. P. Zhu, S. Chen and C. H. Liang, *RSC Adv.*, 2020, **10**, 10921–10931.
25 J. J. Sun, X. Y. Li, Q. D. Zhao, O. Tadéc and S. M. Liu, *Appl. Catal., B*, 2017, **219**, 259–268.
26 Y. Jiang, X. Wang and A. L. Pan, *Adv. Mater.*, 2019, **31**, 1806671.
27 R. Kaur, M. Suresh, J. López-Vidrier, S. Gutsch, C. Weiss, M. Prescher, L. Kirste, R. Singh, B. Pale and M. Zacharias, *New J. Chem.*, 2020, **44**, 19742–19752.
28 M. Shekofteh-Gohari, A. Habibi-Yangjeh, M. Abitorabi and A. Rouhi, *Crit. Rev. Environ. Sci. Technol.*, 2018, **48**, 806–857.
29 M. Pirhashemi, A. Habibi-Yangjeh and S. R. Pouran, *J. Ind. Eng. Chem.*, 2018, **62**, 1–25.
30 A. İ. Vaizoğullar, *Asia-Pac. J. Chem. Eng.*, 2018, **13**, e2154.
31 X. R. Zhang, Y. W. Huo, M. Shakeel, B. S. Li, L. Wang, J. J. Liu and S. L. Zuo, *ChemistrySelect*, 2020, **5**, 1640–1647.
32 X. Q. Liu, H. M. Xu, D. Y. Li, Z. W. Zou and D. S. Xia, *ChemistrySelect*, 2019, **4**, 12245–12251.
33 F. Teng, W. X. Ouyang, Y. M. Li, L. X. Zheng and X. S. Fang, *Small*, 2017, **13**, 1700156.
34 J. Q. Chang, Y. Zhong, C. H. Hu, J. L. Luo and P. G. Wang, *J. Mol. Struct.*, 2019, **1183**, 209–216.